NASA/TM—2018-219962 AIAA–2018–4808

Development Status of a Three-Dimensional Electron Fluid Model for Hall Thruster Plume Simulations

Maria Choi and John T. Yim
Glenn Research Center, Cleveland, Ohio

October 2018

NASA STI Program . . . in Profile

Since its founding, NASA has been dedicated to the advancement of aeronautics and space science. The NASA Scientific and Technical Information (STI) Program plays a key part in helping NASA maintain this important role.

The NASA STI Program operates under the auspices of the Agency Chief Information Officer. It collects, organizes, provides for archiving, and disseminates NASA's STI. The NASA STI Program provides access to the NASA Technical Report Server—Registered (NTRS Reg) and NASA Technical Report Server—Public (NTRS) thus providing one of the largest collections of aeronautical and space science STI in the world. Results are published in both non-NASA channels and by NASA in the NASA STI Report Series, which includes the following report types:

- TECHNICAL PUBLICATION. Reports of completed research or a major significant phase of research that present the results of NASA programs and include extensive data or theoretical analysis. Includes compilations of significant scientific and technical data and information deemed to be of continuing reference value. NASA counter-part of peer-reviewed formal professional papers, but has less stringent limitations on manuscript length and extent of graphic presentations.

- TECHNICAL MEMORANDUM. Scientific and technical findings that are preliminary or of specialized interest, e.g., "quick-release" reports, working papers, and bibliographies that contain minimal annotation. Does not contain extensive analysis.

- CONTRACTOR REPORT. Scientific and technical findings by NASA-sponsored contractors and grantees.

- CONFERENCE PUBLICATION. Collected papers from scientific and technical conferences, symposia, seminars, or other meetings sponsored or co-sponsored by NASA.

- SPECIAL PUBLICATION. Scientific, technical, or historical information from NASA programs, projects, and missions, often concerned with subjects having substantial public interest.

- TECHNICAL TRANSLATION. English-language translations of foreign scientific and technical material pertinent to NASA's mission.

For more information about the NASA STI program, see the following:

- Access the NASA STI program home page at http://www.sti.nasa.gov

- E-mail your question to help@sti.nasa.gov

- Fax your question to the NASA STI Information Desk at 757-864-6500

- Telephone the NASA STI Information Desk at 757-864-9658

- Write to:
  NASA STI Program
  Mail Stop 148
  NASA Langley Research Center
  Hampton, VA 23681-2199

NASA/TM—2018-219962 AIAA–2018–4808

Development Status of a Three-Dimensional Electron Fluid Model for Hall Thruster Plume Simulations

Maria Choi and John T. Yim
Glenn Research Center, Cleveland, Ohio

Prepared for the
Propulsion and Energy Forum
sponsored by the American Institute of Aeronautics and Astronautics
Cincinnati, Ohio, July 9–11, 2018

National Aeronautics and
Space Administration

Glenn Research Center
Cleveland, Ohio 44135

October 2018

Acknowledgments

The authors would like to like to thank the Space Technology Mission Directorate through the Solar Electric Propulsion Technology Demonstration Mission Project for funding this project for the Advanced Electric Propulsion System.

Level of Review: This material has been technically reviewed by technical management.

Available from

NASA STI Program
Mail Stop 148
NASA Langley Research Center
Hampton, VA 23681-2199

National Technical Information Service
5285 Port Royal Road
Springfield, VA 22161
703-605-6000

This report is available in electronic form at http://www.sti.nasa.gov/ and http://ntrs.nasa.gov/

Development Status of a Three-Dimensional Electron Fluid Model for Hall Thruster Plume Simulations

Maria Choi and John T. Yim
National Aeronautics and Space Administration
Glenn Research Center
Cleveland, Ohio 44135

Summary

A three-dimensional (3-D) electron fluid model has been developed as a stepping stone to fully describe the electron current flow across magnetic fields inside a vacuum chamber and to provide electron flux to solar arrays for a spacecraft surface charging model. The physical and numerical models of the electric potential solver, including finite-volume formulation and the treatment of boundary conditions, are presented in this paper. Verification tests of the model are presented.

1.0 Introduction

While electric propulsion (EP) plume models need to accurately predict on-orbit operations of EP thrusters, the models are most often validated through comparisons with experimental data measured in ground-based vacuum facilities. Predicting the behavior of a flight system requires a deep understanding of both component- and system-level interactions, including thruster, cathode, and facility effects, such as background pressure, electrical, and carbon backsputter effects. In order to better understand the testing environment of ground vacuum chambers, which is absent in space, it is critical to understand both the motion of heavy particles in the plume and the movement of bulk electron flows. While the background pressure effects have been extensively studied in the past (Refs. 1 to 6), there is still limited understanding of how electrons in the plume of EP thrusters travel through and interact with the metallic conductive walls of vacuum chambers. Recent studies have suggested that the presence of conducting walls provides alternate pathways for electrons to travel from the cathode and serve as a recombination site (Refs. 7 and 8). This electrical facility effect can become more significant for higher power thrusters operating in vacuum facilities. Since this effect is absent in orbit and simulations are most often validated with the data in these facilities, the transport of electrons in a vacuum chamber needs to be better understood and simulated with more detailed physics.

A conventional way to simulate electrons in the plume of EP thrusters is to assume the Boltzmann relation. This method is simple and useful for isothermal, collisionless, and unmagnetized regions, but has major limitations for Hall thruster plume simulations. First, the electron temperature gradient in the plume is not negligible as it can vary by more than an order of magnitude from the near field to the far field. Second, the magnetic field strength is still strong in the near-field plume as the field leaks into the plume. In order to improve the fidelity of electron model, early work by Boyd and Yim (Ref. 9) demonstrated the viability of using the generalized Ohm's law and steady-state current conservation equation approach to solve for electron current flows for a Hall thruster plume, assuming negligible magnetic fields. This work was further demonstrated on a cluster of Hall thruster plumes by Cai and Boyd (Ref. 10). In both cases, the authors demonstrated the difference in plume structures between their approach and the traditional Boltzmann relation approximation used in plume codes, which enforces exactly zero electron current everywhere in the plume such as the Coliseum tool described by Brieda and VanGilder (Ref. 11). The work in References 9 and 10 was further improved by Choi and Boyd (Ref. 12) by including a full-electron mobility tensor to

account for anisotropies in electron transport in a vacuum chamber due to magnetic field effects. This study used a two-dimensional (2-D) axisymmetric unstructured mesh and showed that the magnetic field effects are non-negligible in the near-field plumes of the anode and cathode.

The present work utilizes a similar formulation by Choi and Boyd (Ref. 12) in a three-dimensional (3-D) structured cell-centered finite volume method. In this paper, the full electron mobility tensor, $\bar{\bar{\mu}}$, from Reference 12, and a full representation of the electron current density, $\mathbf{j}_e$, in 3-D Cartesian grids is developed and presented to better understand the electron transport and current flow in a vacuum chamber. Using the generalized Ohm's law and steady-state current conservation equation, the electric potential is derived. This new electron model has the capability to model electron transport across a complex magnetic field topology in the plume, which includes a magnetic field separatrix and a purely axial component along the cathode centerline axis and a purely radial component near the discharge channel exit, as shown in Figure 1. A detailed description of the physical and numerical models of the electric potential solver, including finite-volume formulation and treatment of boundary conditions, is provided in the paper. Before simulating a full thruster, the model is verified by using the method of manufactured solutions and a mock Hall thruster test case. The accuracy of the new model and effect of the magnetic field in the near-field plume will be discussed.

This model is currently being implemented into a hybrid particle-in-cell (PIC) and fluid framework, known as the Thermophysics Universal Research Framework (TURF), developed by the Air Force Research Laboratory (AFRL) at Edwards Air Force Base (Ref. 13). The present model in TURF framework will ultimately be used to pursue integration modeling of both the ground facility and flight operations. More specifically, the model should be able to (1) map out the electrostatic potential and the electron current flows throughout the chamber volume of a Hall thruster firing in a vacuum chamber and (2) provide the electron current flux to surfaces, which is required for their surface charging model (Ref. 13) that was recently implemented.

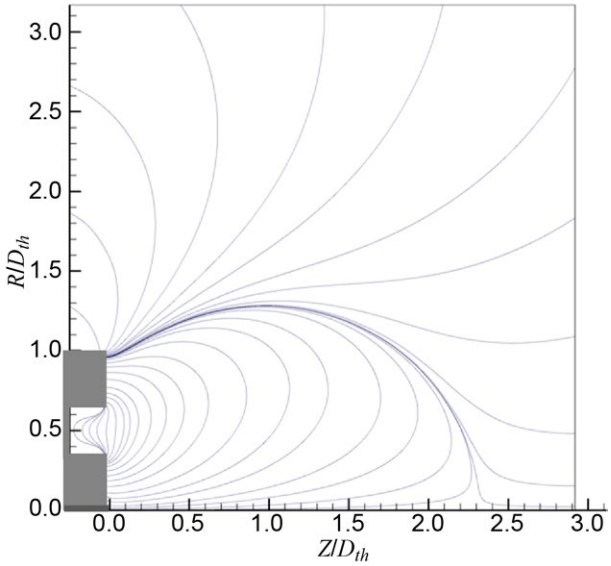

Figure 1.—Complex magnetic field lines in a Hall thruster (Ref. 12), where D_{th} is thruster diameter, R is radial displacement, and Z is axial displacement.

2.0 Physical and Numerical Models

For a fluid description of the electron plasma, the generalized Ohm's law and steady-state current conservation equation are derived as

$$\mathbf{j}_e = \mu_e \left(\mathbf{j}_e \times \mathbf{B} \right) + \sigma_e \left(\mathbf{E} + \frac{1}{en_e} \nabla P_e \right) \tag{1}$$

$$\nabla \cdot \left(\mathbf{j}_e + \mathbf{j}_i \right) = 0 \tag{2}$$

where $\mathbf{j}_e$ and $\mathbf{j}_i$ are the electron and ion current densities, respectively, **B** is the magnetic field, **E** is the electric field, σ_e is the electron conductivity, n_e is the electron number density, P_e is the electron pressure assuming ideal gas, and μ_e is the electron mobility defined as

$$\mu_e = \frac{q}{m_e \nu_{ce}} \tag{3}$$

with q being the elementary charge, m_e the electron mass, and ν_{ce} the total collision frequency of the electron fluid.

Introducing plasma potential ϕ in relation to the electric field, $-\nabla\phi = \mathbf{E}$, Equation (1) can be rewritten as

$$\bar{\bar{\mu}} \mathbf{j}_e = \sigma_e \left(-\nabla\phi + \frac{1}{en_e} \nabla P_e \right) \tag{4}$$

where $\bar{\bar{\mu}}$ is the electron mobility tensor and B_x, B_y, and B_z are the value of the magnetic field in the *x*-, y-, and *z*-directions,

$$\bar{\bar{\mu}} = \begin{bmatrix} 1 & -\mu_e B_x & \mu_e B_z \\ \mu_e B_x & 1 & -\mu_e B_y \\ -\mu_e B_z & \mu_e B_y & 1 \end{bmatrix} \tag{5}$$

Combining Equation (4) with Equation (3) obtains the following equation to solve for the plasma potential:

$$\nabla \cdot \left(\bar{\bar{\mu}}^{-1} \sigma_e \nabla\phi \right) = \nabla \cdot \left(\bar{\bar{\mu}}^{-1} \frac{\sigma_e}{en_e} \nabla P_e \right) + \nabla \cdot \mathbf{j}_i \tag{6}$$

where $\bar{\bar{\mu}}^{-1}$ is the inverse of the electron mobility tensor,

$$\bar{\bar{\mu}}^{-1} = \frac{1}{1 + \mu_e^2 |B|^2} \begin{bmatrix} 1 + \mu_e^2 B_x^2 & \mu_e^2 B_x B_y + \mu_e B_z & \mu_e^2 B_x B_z + \mu_e B_y \\ \mu_e^2 B_x B_y - \mu_e B_z & 1 + \mu_e^2 B_y^2 & \mu_e^2 B_y B_z + \mu_e B_x \\ \mu_e^2 B_x B_z + \mu_e B_y & \mu_e^2 B_y B_z - \mu_e B_x & 1 + \mu_e^2 B_y^2 \end{bmatrix} \tag{7}$$

A cell-centered finite-volume method is used to discretize the governing equation in Equation (6) inside a control volume, *V*,

$$\int_V \left[\nabla\cdot\left(\bar{\bar{\mu}}^{-1}\sigma_e\nabla\phi\right)\right]dV = \int_V \left[\nabla\cdot\left(\bar{\bar{\mu}}^{-1}\frac{\sigma_e}{en_e}\nabla P_e\right)\right]dV + \int_V \left(\nabla\cdot\mathbf{j}_i\right)dV \tag{8}$$

The volume integrals are transformed as surface integrals using Green's theorem. Then, the surface integral is approximated as the sum of all fluxes along all faces. In 3-D, this operation for the left-hand term of Equation (8) will be

$$\begin{aligned}&\sum_{p}^{\text{All faces}} \left(\sigma\bar{\bar{\mu}}^{-1}\nabla\phi\right)_q\cdot\left(\hat{n}dS\right)_q \\ &\quad=\left(\sigma\bar{\bar{\mu}}^{-1}\nabla\phi\right)_e\cdot\left(\hat{n}dS\right)_e+\left(\sigma\bar{\bar{\mu}}^{-1}\nabla\phi\right)_n\cdot\left(\hat{n}dS\right)_n+\left(\sigma\bar{\bar{\mu}}^{-1}\nabla\phi\right)_w\cdot\left(\hat{n}dS\right)_w+\left(\sigma\bar{\bar{\mu}}^{-1}\nabla\phi\right)_s\cdot\left(\hat{n}dS\right)_s \\ &\quad+\left(\sigma\bar{\bar{\mu}}^{-1}\nabla\phi\right)_b\cdot\left(\hat{n}dS\right)_b+\left(\sigma\bar{\bar{\mu}}^{-1}\nabla\phi\right)_f\cdot\left(\hat{n}dS\right)_f\end{aligned} \tag{9}$$

where subscripts *e*, *w*, *n*, *s*, *f*, and *b* represent the east, west, north, south, front, and back faces, repectively. The final discretized form of this equation turns out to be identical to a cell-centered finite-differencing discretization and has 27 stencils in 3-D (Figure 2(a)). After discretization, the equation becomes a linear system of equations:

$$a\phi_{ijk}+b\phi_{i+1,jk}+c\phi_{i-1,jk}+d\phi_{j+1,ik}+e\phi_{j-1,ik}+\cdots+h\phi_{i+1j+1}+i\phi_{i+1j-1}+j\phi_{i-1j+1}+\cdots=F_{ijk} \tag{10}$$

where F_{ijk} is the right-hand side (RHS) term at location *ijk* and all coefficients in front of ϕ's (i.e., *a*, *b*, *c*…) represent flux terms (i.e., $\sigma\bar{\bar{\mu}}^{-1}$) at faces such as *e*, *w*, *n*, *s*, *f*, and *b* as indicated in the red boxes in Figure 2(b).

The electron pressure is assumed to be isotropic and follows the ideal gas law. The ion current density information in each control volume is acquired through the PIC method, assuming quasi-neutrality. The plasma potential is determined by inverting the matrix. After the plasma potential is calculated, the electron current density in Equation (4) can be solved:

$$\mathbf{j}_e=\bar{\bar{\mu}}^{-1}\sigma_e\left(-\nabla\phi+\frac{1}{en_e}\nabla P_e\right) \tag{11}$$

where the central differencing is used to calculate the derivatives.

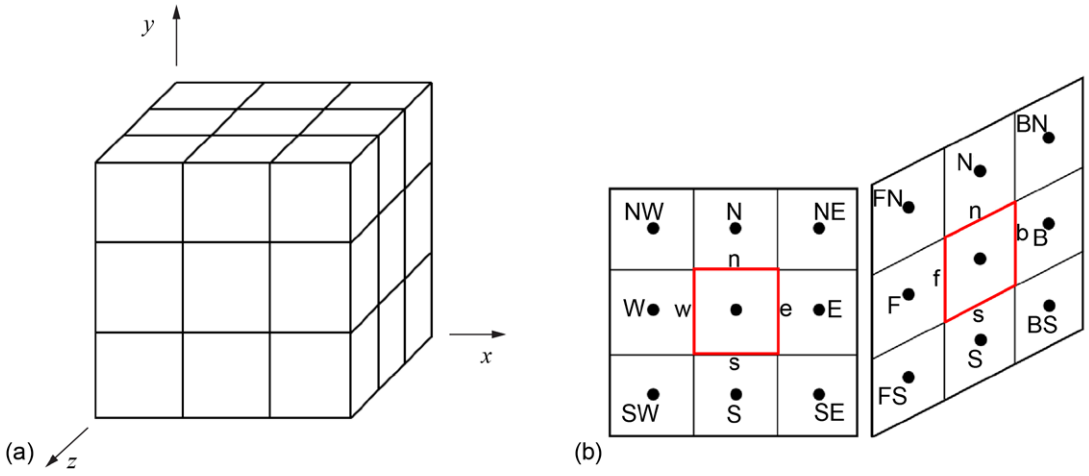

Figure 2.—Electron fluid model with 27-point stencils. (a) 3-D representation. (b) Cell centers and faces.

3.0 Boundary Conditions

In a Hall thruster plume simulation, two types of conditions are typically used: (1) direct value (e.g., all metallic and ground surfaces including the chamber wall) and (2) gradient or flux to the surface (e.g., zero-gradient potential such as a dielectric thruster body), which are the Dirichlet and Neumann boundary conditions, respectively. Although various options of treating these boundary conditions for this model are discussed in this section, not all of these boundary conditions were presented.

3.1 Dirichlet Boundary Condition

There are multiple ways to implement the Dirichlet boundary condition for the plasma potential. The simplest way is to have the surface on the cell center using a ghost cell (e.g., ϕ_0), as shown in Figure 3(a). Then, the known potential value can be incorporated as a boundary condition by moving the boundary term to the RHS of the equation for the interior cells. This method requires modifying all interior cells that have a boundary cell adjacent to them and will result in a matrix with size ($N_x \times N_y \times N_z$) by ($N_x \times N_y \times N_z$), where N_x, N_y, and N_z are the number of cells in *x*-, y-, and *z*-directions. Instead of this incorporation, the boundary terms can be added in the matrix as additional rows, which preserves the matrix shape of interior cells but increases the matrix to [($N_x + 2$) × ($N_y + 2$) × ($N_x + 2$)] by [($N_x + 2$) × ($N_y + 2$) × ($N_x + 2$)].

When the Dirichlet condition is imposed on a cell face instead of a cell center, as shown in Figure 3(b), either the finite-volume approach or finite-difference approach can be taken. For the finite-volume approach, forward differencing can be at the boundary surface (e.g., $x = \frac{1}{2}$ in Figure 3(b)) used as

$$\left.\frac{\partial \phi}{\partial x}\right|_{\frac{1}{2}} = \frac{\phi_1 - \phi_{\frac{1}{2}}}{\left(\frac{\Delta x}{2}\right)} \tag{12}$$

For the finite-difference approach, the ghost cell, ϕ_0, is used and its value is replaced by a known potential value at the wall (i.e., $\phi_{\frac{1}{2}}$), which is approximated using Taylor's expansion. In this study, both first- and second-order extrapolations are tested and defined as

$$\phi_0 = 2\phi_{\frac{1}{2}} - \phi_1 \tag{13}$$

and

$$\phi_0 = \frac{8}{3}\phi_{\frac{1}{2}} - 2\phi_1 + \frac{1}{3}\sigma_2 \tag{14}$$

respectively. When approximating the flux at the boundary cell face, $\left(\sigma\bar{\bar{\mu}}^{-1}\right)_{\frac{1}{2}}$, a second-order extrapolation is used:

$$\left(\sigma\bar{\bar{\mu}}^{-1}\right)_{\frac{1}{2}} = \frac{3\left(\sigma\bar{\bar{\mu}}^{-1}\right)_1 - \left(\sigma\bar{\bar{\mu}}^{-1}\right)_2}{2} \tag{15}$$

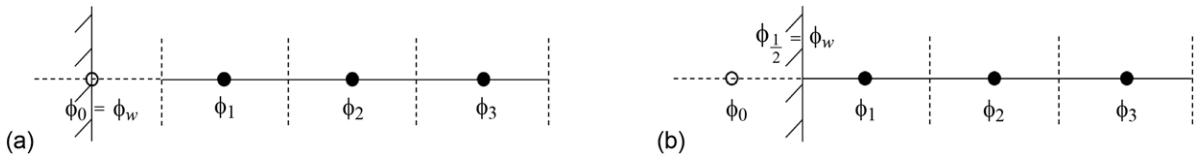

Figure 3.—Two types of Dirichlet conditions. (a) A solid surface lying on cell center. (b) A solid surface lying on cell face.

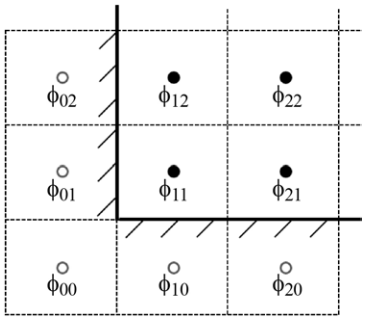

Figure 4.—Neumann boundary condition using ghost cells.

With a corner cell, as shown in Figure 4, the corner ghost cell, ϕ_{00}, has to be approximated. The simplest approach would be to use distance-weighted averaging. The two- and three-point averaging are as shown here:

$$\phi_{00} = \frac{\phi_{10}\Delta y + \phi_{01}\Delta_x}{\Delta x + \Delta y} \tag{16}$$

$$\phi_{00} = \frac{\phi_{10}\Delta y + \phi_{01} r\Delta_x + \phi_{11}\Delta x\Delta y}{\Delta x + \Delta y + r} \tag{17}$$

where $r = \sqrt{\Delta x^2 + \Delta y^2}$. When $\Delta x = \Delta y$, the two-point distance averaging becomes $\phi_{00} = 0.5\left(\phi_{10} + \phi_{01}\right)$, and substituting the first- and second-order extrapolations gives the following:

$$\phi_{00} = \phi_{1\frac{1}{2}} + \phi_{\frac{1}{2}1} - \phi_{11} \tag{18}$$

and

$$\phi_{00} = \frac{1}{2}\left[\frac{8}{3}\left(\phi_{\frac{1}{2}1} + \phi_{1\frac{1}{2}}\right) - 4\phi_{11} + \frac{1}{3}\left(\phi_{12} + \phi_{21}\right)\right] \tag{19}$$

3.2 Neumann Boundary Condition

As illustrated in Figure 5, the Neumann boundary condition is where the normal component of the potential gradient, or the electric field, is known at a cell face. In this 1-D case (Figure 5(a)), the ghost cell, ϕ_0, is replaced by the known gradient at the cell face as $\phi_0 = \phi_1 + g_w\Delta x$, which is then used to modify the matrix. For a zero-gradient condition, a mirror condition can be used by setting $\phi_0 = \phi_1$.

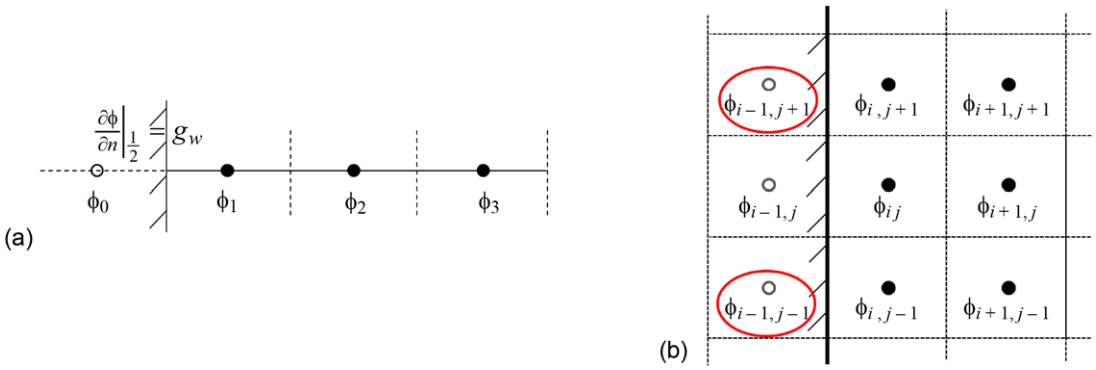

Figure 5.—Neumann boundary conditions. (a) One-dimensional. (b) Two-dimensional.

For a 3-D case, the treatment of this condition is slightly more involved due to mixed derivative terms. Figure 5(b) illustrates this condition in 2-D with a solid surface boundary on the left side of the domain, where $\phi_{i-1,j+1}$ and $\phi_{i-1,j+1}$ in addition to ϕ_{ij} having to be replaced in terms of the interior cells. The surface integral of the west-side face with a zero-gradient condition (i.e., $\frac{\partial\phi}{\partial x} = g_w \neq 0$) for this case in 3-D yields

$$\begin{aligned}\left(\sigma\bar{\bar{\mu}}\nabla\phi\right)\big|_w\cdot(A)_w &= \left(\sigma\mu_{11}\frac{\partial\phi}{\partial x}+\sigma\mu_{12}\frac{\partial\phi}{\partial y}+\sigma\mu_{13}\frac{\partial\phi}{\partial z}\right)_w(A)_w \\ &= \left(\sigma\mu_{11}g_w+\sigma\mu_{12}\frac{\phi_{i,j+1}-\phi_{i,j-1}}{2\Delta y}+\sigma\mu_{13}\frac{\phi_{i,k+1}-\phi_{i,k-1}}{2\Delta z}\right)\Delta y\Delta z\end{aligned} \tag{20}$$

where $g_w\Delta x$ terms were cancelled out, and A is the area. Integrals of all other remaining faces that include $\phi_{i-1,j+1}$ and $\phi_{i-1,j-1}$ should also account for the gradient terms appropriately.

4.0 Verification Tests

Before implementing this model into a Hall thruster plume code, the model and algorithm have to be tested and verified. In this section, the method of manufactured solutions and a Hall thruster-like test case are used to verify the model and algorithm.

4.1 Method of Manufactured Solutions

In order to verify the numerical model, the method of manufactured solutions is used. In this study, the new model is tested using various types of functions as manufactured (exact) solutions, including polynomial, sinusoidal, and exponential solutions, or some combination of these. The manufactured solution is substituted into the governing equation being solved numerically, and the source term in the RHS is acquired that satisfies this solution. As an example, one of the manufactured solutions tried is shown here:

$$\phi_{\text{exact}} = \frac{K}{6}\left(x^2+y^2+z^2\right) \tag{21}$$

where $K = 3$, and the RHS is

$$F = \frac{K}{3}\sigma_e\left(\mu_{11} + \mu_{22} + \mu_{33}\right) \tag{22}$$

The numerical and exact solutions are compared in Figure 6. The numerical solution calculated using the new model qualitatively reproduces the exact solution very well.

For more quantitative study, a grid convergence study can be performed using the L_2-norm error:

$$\left\|e\right\|_{L_2} = \sqrt{\sum_{k=1}^{N_k} \int_{\Omega_k} \left(\phi_h - \phi_{\text{exact}}\right)^2 d\Omega_k} \tag{23}$$

where ϕ_h is the numerical value of the plasma potential and ϕ_{exact} is the true solution. The convergence study is performed as shown in Figure 7, which confirms the second-order accuracy, as indicated by the slope of the linear plot (≈–2).

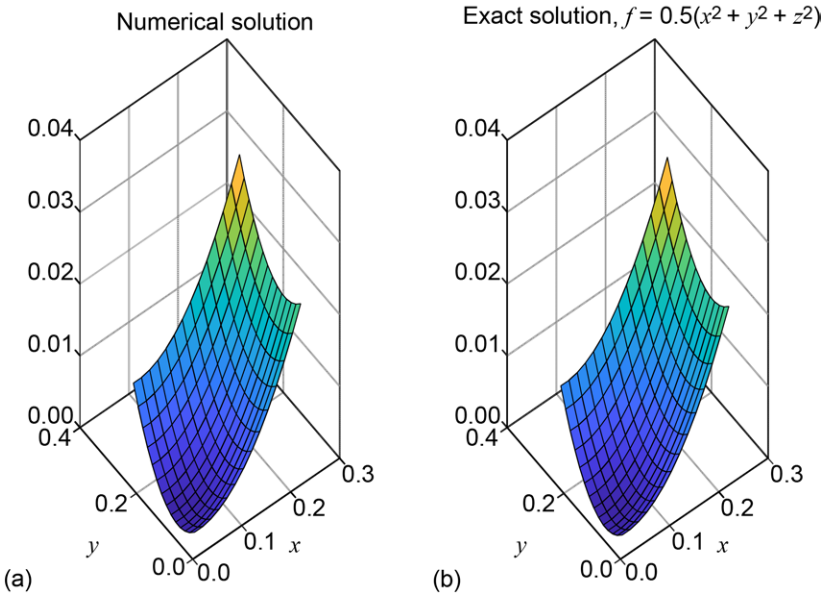

Figure 6.—Qualitative comparison of solutions. (a) Numerical solution. (b) Exact (manufactured) solution $\phi = 0.5(x^2 + y^2 + z^2)$.

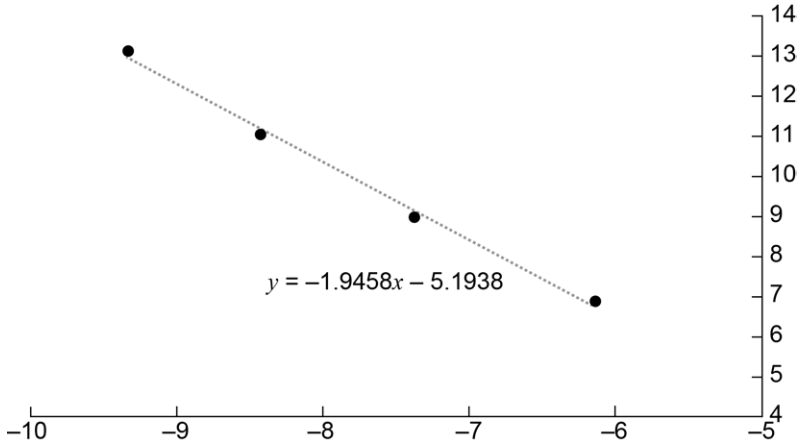

Figure 7.—Grid convergence study of the current model.

4.2 A Hall Thruster-Like Test Case

Before implementing this model into a Hall thruster plume simulation code, a Hall thruster-like test case was constructed by Dragnea, Hara, and Boyd using a similar 2-D axisymmetric hybrid model (Ref. 14). Figure 8 shows the strength of the magnetic fields applied throughout the computational domain. The field is radial only. Fixed plasma potentials of 300 and 0 V at the left (anode-like) and the right (cathode-like) boundaries, respectively, and zero-gradient conditions were applied at the top and the bottom boundaries (Figure 9(a)). Constant electron temperature (T_e = 25 eV) and electron number density ($n_e = 1\times10^{17}$ m^{-3}) were used. Since the current model is in 3-D, infinitely long boundaries were assumed in the z-direction. Figure 9 shows the plasma potential calculated using (a) 2-D axisymmetric model solution that serves as a true solution and (b) 3-D finite-volume model developed in this study.

Using the plasma potential fields calculated, the electron current densities in Equation (4) can be determined. The finite-difference scheme is used to perform this operation, and the result is shown in Figure 10.

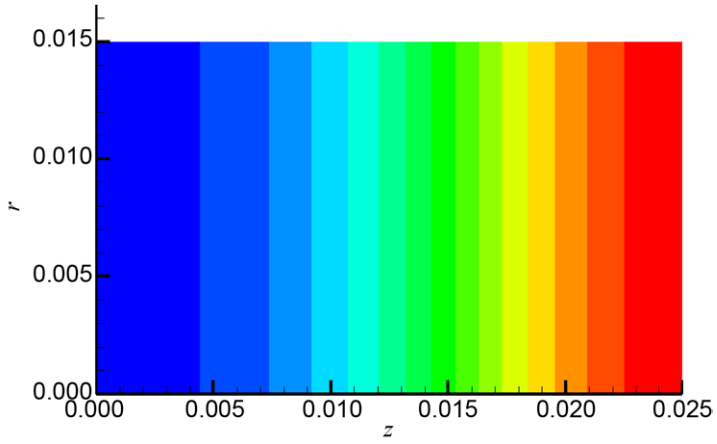

Figure 8.—Hall thruster-like test setup showing magnetic field strength.

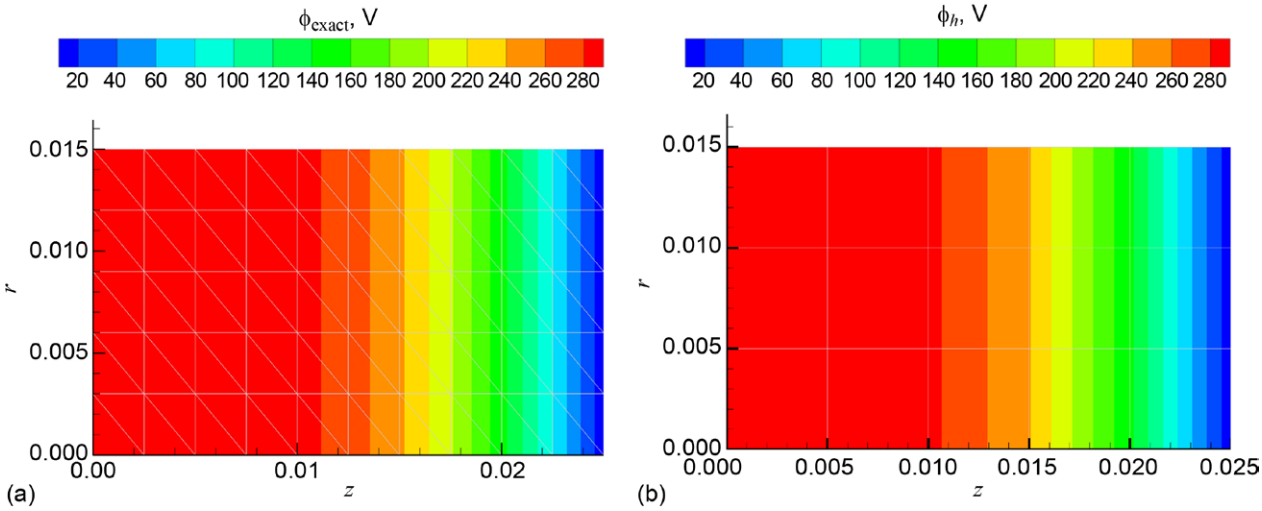

Figure 9.—Calculated plasma potential. (a) Using two-dimensional axisymmetric finite element model from Ref. 12. (b) Using three-dimensional rectangular finite volume model in this study with constant values in z-direction.

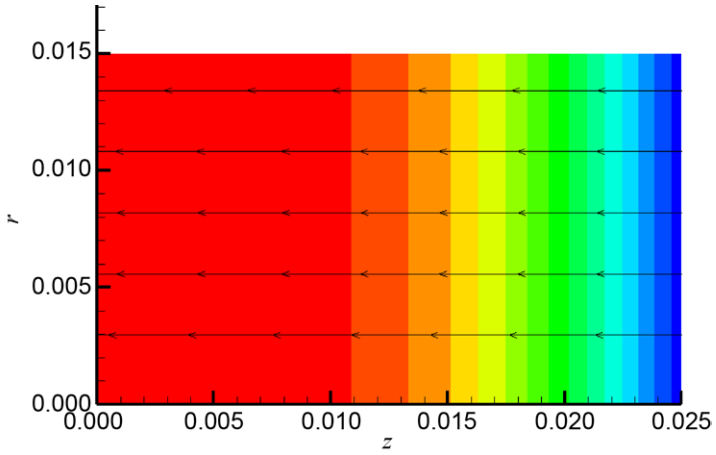

Figure 10.—Electron current density streamline.

5.0 Conclusions

A three-dimensional (3-D) electron fluid model has been developed as a stepping stone to ultimately better understand the electrical facility effects in a conducting vacuum chamber and to provide electron flux to solar arrays for spacecraft surface charging model in Thermophysics Universal Research Framework. This unique formulation can include a representative magnetic field throughout an entire vacuum chamber domain for future Hall thruster plume simulations. This paper described the derivation and verification of the plasma potential solver. While not all of them were used, various types of boundary condition treatments were derived and presented. Ongoing activities include studying the effects of various boundary condition types and conducting further verification tests with various magnetic field strengths and topologies.

In the near future, this model, combined with a steady-state and/or transient electron energy equation, will be implemented in the research framework and used to simulate a Hall thruster plume in both a full vacuum chamber at Glenn and on-orbit with spacecraft geometry.

Appendix—Nomenclature

1-D	one-dimensional
2-D	two-dimensional
3-D	three-dimensional
AFRL	Air Force Research Laboratory
EP	electric propulsion
PIC	particle-in-cell
RHS	right-hand side
TURF	Thermophysics Universal Research Framework

Symbols

A	area
$\mathbf{B}$	magnetic field
B_x	value of magnetic field in x-direction
B_y	value of magnetic field in y-direction
B_z	value of magnetic field in z-direction
D_{th}	thruster diameter
e	electron charge
$\mathbf{E}$	electric fields
F	right-hand side term
g_w	flux
$\mathbf{j}_e$	electron current density
$\mathbf{j}_i$	electron ion density
K	constant coefficient
m_e	electron mass
$\hat{n}$	normal vector
n_e	electron number density
N_x	number of cells in the x-direction
N_y	number of cells in the y-direction
N_z	number of cells in the z-direction
P_e	electron pressure
q	elementary charge
R	radial displacement
S	surface
T_e	electron temperature
V	cell volume
Z	axial displacement
ϕ	plasma potential
ϕ_0, ϕ_{00}	ghost cells
ϕ_{exact}	true solution
ϕ_h	numerical solution
ϕ_w	wall potential
μ_e	electron mobility
$\bar{\bar{\mu}}$	full electron mobility tensor

$\bar{\bar{\mu}}^{-1}$ inverse of electron mobility tensor

ν_{ce} total collision frequency of electron fluid

σ_e electron conductivity

Subscripts

b back face

e east face

f front face

i index in *x*-direction

j index in *y*-direction

k index in *z*-direction

n north face

s south face

w west face

References

1. Walker, Mitchell L.R.; Hofer, Richard R.; and Gallimore, Alec D.: The Effects of Nude Faraday Probe Design and Vacuum Facility Backpressure on the Measured Ion Current Density Profile of Hall Thruster Plumes. AIAA 2002–4253, 2002.
2. Walker, Mitchell L.R, et al.: Effect of Backpressure on Ion Current Density Measurements in Hall Thruster Plumes. J. Propul. Power, vol. 21, no. 3, 2005, pp. 408–415.
3. Walker, Mitchell Louis Ronald: Effects of Facility Backpressure on the Performance and Plume of a Hall Thruster. Ph.D. Dissertation, Univ. of Michigan, 2005.
4. Reid, Bryan Michael: The Influence of Neutral Flow Rate in the Operation of Hall Thrusters. Ph.D. Dissertation, Univ. of Michigan, 2009.
5. Kamhawi, Hani, et al.: Investigation of the Effects of Facility Background Pressure on the Performance and Voltage-Current Characteristics of the High Voltage Hall Accelerator. AIAA 2014–3707, 2014.
6. Huang, Wensheng, et al.: Effect of Background Pressure on the Plasma Oscillation Characteristics of the HiVHAc Hall Thruster. AIAA 2014–3708, 2014.
7. Frieman, Jason D., et al.: Electrical Facility Effects on Hall Thruster Cathode Coupling: Performance and Plume Properties. J. Propul. Power, vol. 32, no. 1, 2016, pp. 251–264.
8. Frieman, Jason D., et al.: Role of a Conducting Vacuum Chamber in the Hall Effect Thruster Electrical Circuit. J. Propul. Power, vol. 30, no. 6, 2014, pp. 1471–1479.
9. Boyd, Iain D.; and Yim, John T.: Hall Thruster Plume Simulation Using a Detailed Hybrid Model. AIAA 2004–3952, 2004.
10. Cai, Chunpei; and Boyd, Iain D.: 3D Simulation of Plume Flows From a Cluster of Plasma Thrusters. AIAA 2005–4462, 2005.
11. Brieda, Lubos; and VanGilder, Douglas: Multi-Domain Plasma Expansion Simulations Using a Particle-in-Cell Method. AIAA 2006–5023, 2006.
12. Choi, M.; and Boyd, I.D.: Hybrid Simulation of Magnetic Field Effects in the Plume of a Hall Thruster. Presented at Space Propulsion, Rome, 2016.
13. Araki, Samuel J.; and Barrie, Alexander C.: Electric Propulsion Plume Simulation Coupled With Spacecraft Charging. AIAA 2018–4906, 2018.
14. Dragnea, Horatiu C.; Hara, Kentaro; and Boyd, Iain D.: Development of a 2D Axisymmetric Electron Fluid Model in Hall Thrusters. AIAA 2017–4632, 2017.